

In situ lower crustal accretion by melt sill injection revealed by seismic layering

Peng Guo (✉ pengguo.geos@gmail.com)

CSIRO <https://orcid.org/0000-0003-1248-5650>

Satish Singh

Institut De Physique Du Globe De Paris <https://orcid.org/0000-0002-4594-801X>

Venkata Vaddineni

Laboratoire de Géosciences Marines, Institut de Physique du Globe de Paris

Ingo Grevemeyer

GEOMAR, Helmholtz Centre for Ocean Research <https://orcid.org/0000-0002-6807-604X>

Erdinc Saygin

Deep Earth Imaging Future Science Platform, CSIRO <https://orcid.org/0000-0003-4666-0955>

Article

Keywords: lower crustal accretion, melt sill injection, seismic layering, lower oceanic crust

Posted Date: April 2nd, 2021

DOI: <https://doi.org/10.21203/rs.3.rs-145281/v1>

License:  This work is licensed under a Creative Commons Attribution 4.0 International License.

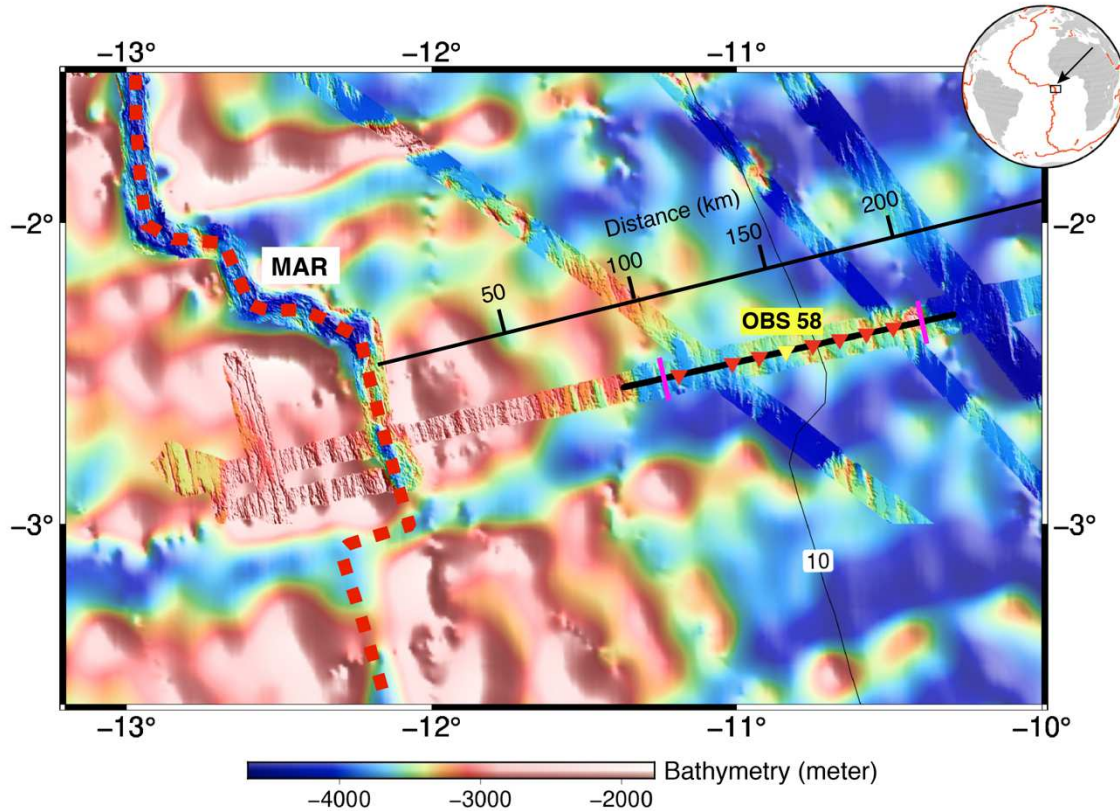
[Read Full License](#)

Version of Record: A version of this preprint was published at Nature Geoscience on June 13th, 2022. See the published version at <https://doi.org/10.1038/s41561-022-00963-w>.

27 by melt sill intrusions beneath the ridge axis is a stable process. We also find that the
28 upper crust is ~400 m thinner than that from conventional travel-time analysis. Taken
29 together, these discoveries suggest that the magmatism plays more important roles in the
30 crustal accretion process at slow spreading ridges than previously realised, and that in-
31 situ lower crustal accretion is the main process for the formation of lower oceanic crust.

32

33 Our study area lies in the equatorial Atlantic Ocean (Fig. 1). The equatorial Atlantic Ocean
34 opened during the Late Jurassic, sundering Gondwanaland and separating northern South
35 America from Africa. After break-up, seafloor spreading occurred along the slow spreading
36 Mid-Atlantic Ridge, forming up to 120 Ma old oceanic crust. Half spreading rate to the south
37 of the equator remained in the order of $\sim 16 \text{ mm/year}^{12}$ over the last 20 Myr.

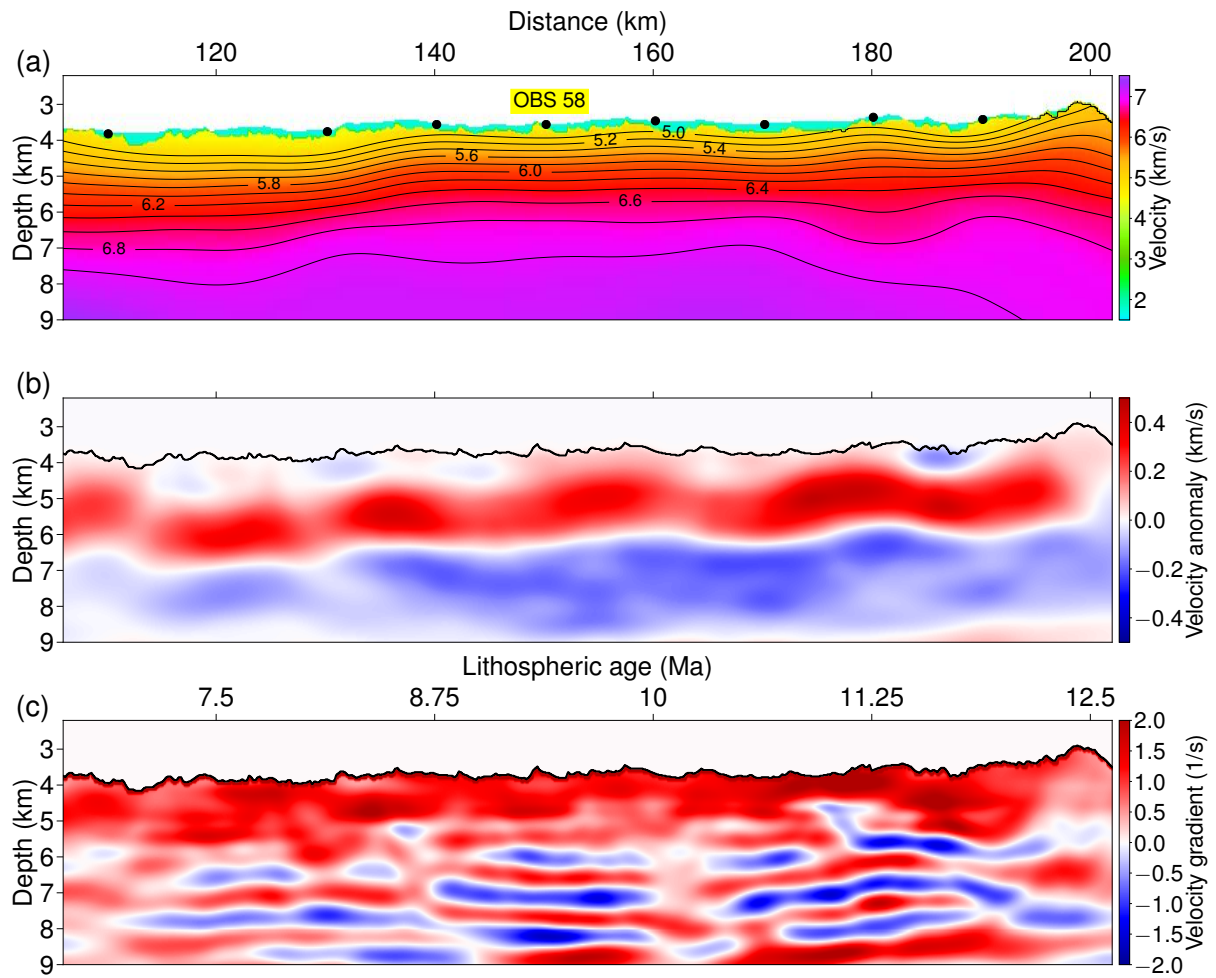


38

39 **Fig. 1: Study Area:** The ocean bottom seismometer (OBS) seismic survey near the Mid-
40 Atlantic Ridge (MAR) in the equatorial Atlantic Ocean. The dashed red line refers to the
41 MAR, and the triangles show the locations of the OBSs used for this study. OBS 58 (yellow
42 triangle) is labelled, with the seismograms shown in Fig. 3. The bold black line passing
43 through OBSs shows the part of shot profile used, and the two pink bars indicate the
44 boundaries of the seismic images shown in Fig. 2. The thin black line and numbers indicate
45 the distance from the MAR. The contour labelling 10 indicates the 10 Ma lithospheric age.
46 See the inset map for the location of the study area.

47

48 In 2017, wide-angle seismic data were acquired aboard the German R/V Maria S. Marian. An
49 air gun array with a total volume of 5440 cubic inch was fired at ~400 m interval, which was
50 recorded on ocean bottom seismometers (OBSs) deployed at a spacing of 10 to 20 km on the
51 seafloor. The crustal (Pg), mantle arrivals (Pn) and wide-angle reflections from the Moho
52 (PmP) were used to obtain the large-scale P-wave velocity structures¹³. Here, we use a part
53 of these data (8 OBSs) where the OBS spacing was dominantly ~10 km (Fig. 1), covering ~7
54 to 12 Ma old seafloor. Fig. 2a shows the velocity model obtained using the travel-time
55 tomography¹³ (see Methods), which was used as the starting velocity model for the full
56 waveform inversion^{14,15} (FWI, see Methods). The crustal thickness in the study area is $5.8 \pm$
57 0.2 km¹³. As expected, the tomographic velocity model contains only the large-scale velocity
58 structures but clearly showing a high velocity gradient upper crust down to ~2.4 km below
59 the basement underlain by a low velocity gradient lower crust.



60

61 **Fig. 2: Velocity Models:** (a) The tomographic seismic velocity model¹³ serves as the starting

62 model for the FWI, (b) the velocity anomaly (the difference between the velocity models

63 from FWI and tomography) from the trace-normalised FWI¹⁴, and (c) the vertical velocity

64 gradient (the derivative of velocity with respect to depth) from the ‘true amplitude’ FWI¹⁵.

65 Black dots in (a) mark the OBS locations. The velocity contours are from 5 to 7 km/s with an

66 increment of 0.2 km/s. The coloured parts in (b) and (c) start from the basement (the top of

67 Layer 2). The lithospheric age in (c) is calculated using a spreading rate of 16 mm/year¹².

68 More images of the oceanic crustal velocity models from FWI can be found in Figs. S3 and

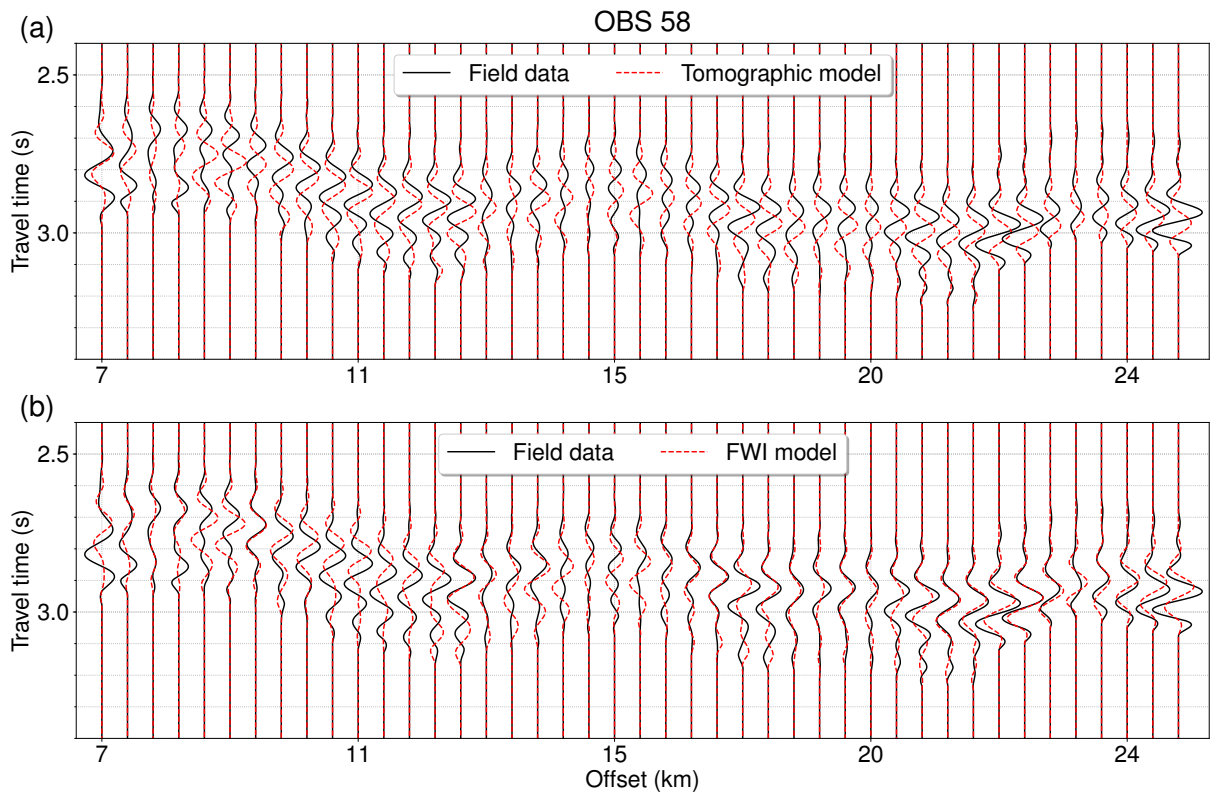
69 S4. The horizontal distance starts with 0 km from the MAR.

70

71

72

73 Fig. 2b shows the velocity anomaly obtained using the trace-normalised FWI¹⁴ (see
74 Methods), which indicates an overall increase in the velocity (Figs. 2b, S3) (positive velocity
75 anomaly) above 6-7 km depth and a decrease in velocity (negative velocity anomaly) below
76 this depth, suggesting that the velocity in the upper crust is 200-400 m/s higher than those
77 obtained from the tomographic method and is 100-300 m/s lower in the lower crust. Starting
78 from this velocity model, we performed the true-amplitude FWI¹⁵ (see Methods) (Figs. 2c,
79 S4). There are alternate high and low velocity layers in the lower crust below ~6 km depth in
80 the vertical velocity gradient image (Figs. 2c, 4a). The synthetically calculated data after the
81 FWI show a much better match to the crustal Pg arrivals of the field data than those from the
82 tomographic model (Figs. 3, S7-S10).



83

84 **Fig. 3: Data comparison for OBS 58:** (a) The field data (black) and the synthetic waveform
85 (red) using the tomographic model (Fig. 2a), and (b) the field data (black) and the synthetic
86 waveform (red) using the true-amplitude FWI model (Fig. S4a). Seismic waveforms from

87 more OBSs can be found in Figs. S7-S10. A reduced travel time of 7 km/s velocity was
88 applied to both the field and synthetic data for plotting purpose.

89

90 In order to make sure that these results from inverting Pg arrivals represent real crustal
91 features, we performed extensive simulated inversion tests with different structures
92 embedded in the model. Synthetic data were computed and then were inverted using the same
93 parameters as the field data inversion (see Methods, Figs. S12-S24). These tests suggest that
94 the layered velocity model in the lower crust is required by the data, and hence they are real
95 structures in the sub-surface. As the dominant frequency in the data is 3.5-10 Hz, the
96 dominant wavelength is 700-1500 m for a velocity of 6.8 km/s, indicating that the vertical
97 resolution in the lower crust is $\sim 400 \text{ m}^{15}$, hence the structures we observed are well resolved.

98 One-dimensional velocity profiles (Figs. 4a, S5-S6) show three distinct features: (1) a layer
99 with a much higher vertical velocity gradient than that of the tomographic model from the
100 basement down to $\sim 1.2 \text{ km}$ depth, where the velocity linearly increases from an average of
101 $\sim 4.8 \text{ km/s}$ at the top to 6.2 km/s at its base, (2) an underlying medium velocity gradient layer
102 of 600-800 m thickness, with the velocity increasing to $\sim 6.6 \text{ km/s}$, and (3) alternating high
103 and low velocity layers (400-600 m thick) with a velocity variation of $\pm 100 - 200 \text{ m/s}$ in the
104 lower crust extending over 10-20 km distance along the profile.

105 The upper high velocity gradient layer is probably associated with the high velocity gradient
106 generally observed at the lava flow-dike (layer 2A/2B) boundary¹⁶, where the rapid velocity
107 increase mainly comes from the collapsing and filling of cracks/pores from lithostatic
108 pressure and hydrothermal precipitation^{16,17}. A recent tomographic study using ultra-long
109 streamer data indicates that this boundary lies at 600 - 800 m below basement for $\sim 7-12$
110 Ma⁹, suggesting a shallower 2A/2B transition than our results. However, these authors found

111 the lava flow-dike boundary at ~ 900 m below the seafloor beneath the ridge axis⁹. The
112 relatively limited offset and low resolution of the tomographic inversion might be the cause
113 of this discrepancy.

114 Generally, the upper and lower crust boundary is defined by a change in the vertical velocity
115 gradient; high velocity gradient in the upper crust with very low gradient in the lower
116 crust^{3,8,17}. Using this definition, the upper crust-lower crust boundary will be at 2.2-2.4 km
117 below basement in the tomographic model and at 1.8-2.0 km in the FWI results (Figs. 4a, S5-
118 S6), suggesting that the upper crust is ~ 400 m thinner (20%) than that based on the travel
119 time analysis, but is consistent with the average thickness of 1.9 km for old (> 7.5 Ma) upper
120 crust from slow-spreading ridges³. Consequently, the lower crust (Layer 3), which mainly
121 consists of gabbro, would be much thicker, suggesting that magmatic process may play a
122 more important role in crustal accretion than previously realised². The average velocity at the
123 top of the lower crust is 6.6 km/s, which is well within the range of 6.56-6.7 km/s estimated
124 from historic surveys³.

125 The alternating high and low velocity layers below ~ 2 km depth from basement in the lower
126 crust could be explained by the presence of (1) gabbro sills within emplaced mantle
127 peridotite^{4,5,18}, (2) hydrothermal alteration¹⁹, or (3) multiple injection and freezing of melt
128 sills of different types of melt in the lower crust beneath the ridge axis^{20,21}.

129 The observation of clear wide-angle Moho reflections (PmP, Fig. S2) on all the OBSs
130 requires the presence of a distinct Moho at ~ 5.8 km below the basement¹³, indicating that the
131 Moho is a petrological boundary separating the gabbroic crust above the mantle peridotite.
132 Furthermore, the tomographic results indicate that velocity in the lower crust increases from
133 ~ 6.6 km/s at 2 km below the basement to ~ 7 km/s just above the Moho, suggestive of a
134 gabbroic origin. The velocity in the mantle just below the Moho is ~ 8 km/s, confirming the

135 presence of mantle peridotite¹³. Additionally, the velocities in the high velocity layers of
136 lower crust are too low to represent serpentinised peridotite. Taken together, these results
137 suggest that the observed lower crustal seismic layering is not due to the presence of gabbro
138 sills in uplifted mantle peridotite.

139 Previous seismic investigation¹⁹ has imaged a 150-200 m thick low-velocity zone above the
140 roof of the axial melt lens (AML), which was interpreted to be formed from enhanced
141 hydrothermal alteration¹⁹. Therefore, the topmost low velocity layer might be associated with
142 this enhanced hydrothermal circulation.

143 Multiple magma lenses in the lower crust have been recently discovered through modern
144 seismic surveys at the fast²²⁻²⁴ and intermediate spreading ridges^{25,26}, supporting the idea of
145 in-situ magma intrusion and crystallisation in the lower crust. However, no such secondary
146 lower crustal melt sills have been observed beneath slow spreading ridges, although low
147 velocity anomalies have been reported in the lower crust, suggestive of the presence of partial
148 melt (mush)^{8,27}. The absence of melt sill evidence beneath slow spreading ridges could be
149 either due to rough seafloor hindering seismic imaging or because of low velocity contrasts
150 between the host mush and the injected melt sills.

151 The layering in the lower crust has been observed in exposed ophiolites. In the Oman
152 ophiolite, which is a representative of fast spreading crust, thin layers (cm to 100 m) of
153 alternating strata rich in mafic minerals (olivine and clinopyroxene) and plagioclase have
154 been observed^{20,21,28}. The analysis of these layers suggests that the lower crust could be
155 formed by cooling and crystallisation of melt sills in situ (the sheeted sill model^{20,21}). In the
156 Bay of Islands ophiolite, a representative of slow spreading environment, layers with
157 thickness of several hundred meters to a kilometer have been observed²⁹.

158 A more than 1500-m of the lower crustal gabbro was drilled during the Ocean Drilling
159 Program Hole 735B^{30,31}, containing several layered units of >250 m thickness. Analysis of a
160 geochemical unit in the lower gabbro³¹ suggests that it constitutes of a single magma
161 reservoir but is separated in two parts. The lower part is formed by a stack of repeated
162 recharge of primitive thin melt sills, whereas the upper part consists of a homogeneous
163 evolved magma mush formed by upward reactive porous flow, progressive differentiation
164 and accumulation^{31,32}. This process would lead to a layering in the lower crust, containing
165 olivine-rich gabbro and troctolites at the base with a distinct boundary separating more
166 evolved olivine and olivine-bearing gabbro with decreasing olivine and increasing
167 plagioclase³¹.

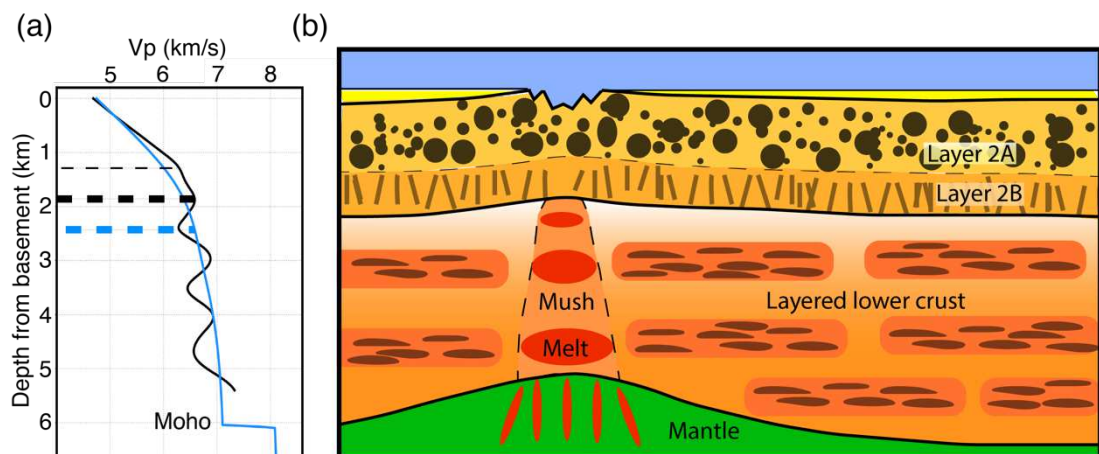
168 Observations from IODP/ODP drilling and ophiolites²⁸⁻³³ indicate that the lower crustal
169 gabbroic rocks are mainly composed of olivine (Ol), clinopyroxene (Cpx), and plagioclase
170 (Pl), with seismic velocities $V_{Ol} > V_{Cpx} > V_{Pl}$ (Table S1), where V represents the velocity.
171 Rocks rich in Ol and Cpx, indicative of more primitive melt, would have higher velocities,
172 whereas those of more evolved rocks rich in Pl would have relatively lower velocities^{33,34}.
173 Using the Voigt-Reuss-Hill averaging method (See Methods), we computed the P-wave
174 velocities for different gabbro compositions from the Hole 735B, and found that the velocity
175 of the gabbro varies from 6.6 km/s to 7.1 km/s (Table S2), for 10% - 20% changes in Ol/Cpx
176 and Pl contents. Therefore, high-velocity layers may contain gabbroic rocks with relatively
177 high Ol/Cpx concentration (usually >10%) such as Ol and Ol-rich gabbro; low-velocity layer
178 may be rich in rocks with low Ol/Cpx (<10%) and high Pl contents, such as Ol-bearing
179 gabbro.

180 The observed lower crustal layering extends over 10-20 km horizontal distance along the
181 profile (Fig. 2c), suggesting that the crustal accretion process by sill injection is stable for up

182 to a million year. A sustained melt supply and a relatively stable crustal accretion process can
183 indeed be a general phenomenon at slow-spreading ridges, especially when the process is not
184 interrupted by the presence of detachment faults^{4,5}, which seems to be the case in our study
185 region; otherwise the layered structure would be more discontinuous. Further, bathymetric
186 data show simple abyssal hill fabrics indicating a normal mode of seafloor spreading. A
187 robust and stable magma supply is also consistent with the estimated thick lower crust. It is
188 also possible that these interpreted frozen sills are thinner and shorter, but our data do not
189 have the resolution to image them, and higher resolution seismic data would be required.

190 Our discovery of layering in the lower crust at the slow-spreading MAR provides important
191 implications for the crustal accretion process, indicating that melt sills in the lower may be
192 more prevalent than previously realised. Fig. 4b shows a schematic diagram about the
193 geometry of the melt lens and the oceanic crust. The discovery of stacked-layering off axis
194 firmly confirms that the lower oceanic crust is formed by the crystallisation of melt sills in
195 situ by multiple injections of upwelling magma from the mantle²¹, not just in the upper axial
196 melt lens then subsiding to greater depths as suggested by the gabbro glacier model³⁵. The
197 alternating high and low velocities indicates the progressive extraction and assimilation of
198 cyclically replenished melts. The high-velocity layers are likely to be formed from primitive
199 melt intrusions at the base of a magma reservoir, whereas the low-velocity layers can be
200 produced by the fractional crystallisation and accumulation of more-evolved, upward-
201 migrated melt residue (mush). In situ crystallisation requires extensive seawater circulation
202 down to the Moho depth along the sides of crystal-rich mush zone beneath the magma
203 chambers for cooling³⁴, which can be provided through well-developed faults in the slow-
204 spreading environment³¹. Moreover, the hydrothermal activities and the magmatic reaction
205 with host rocks could lead to remelting and assimilation, altering the petrological constituents
206 of igneous rocks^{31,32}, hence changing the rock properties further.

207 Our results provide the first seismic image for a layered lower oceanic crust away from
 208 spreading centres. We suggest that, similar to continental lower crust³⁶, the oceanic lower
 209 crust is generally composed of high and low velocity layers, in contrast to the presumed
 210 homogeneous gabbroic lower crust or the presence of mantle peridotite in the lower crust.
 211 The existence of layering in the lower crust provides a strong evidence that magmatism is the
 212 main driving force for the crustal accretion process at slow spreading mid-oceanic ridges, and
 213 that the normal oceanic lower crust is primarily formed by in situ cooling and crystallisation
 214 of cyclic magma upwelling from the upper mantle. Furthermore, the amount of melt
 215 produced in the mantle should be much larger, and hence the mantle must be much hotter or
 216 melt extraction is much more efficient beneath slow spreading ridges than previously
 217 realised.



218
 219 **Fig. 4: Layering in the lower crust:** (a) One-dimensional velocity-depth profiles at the
 220 distance of 182 km from the MAR, derived from tomography (blue) and FWI (black),
 221 respectively. The thin dashed black line is the interpreted boundary of Layer 2A/2B from the
 222 FWI model; the bold dashed blue and black lines indicate the boundaries of Layer 2/3 from
 223 the tomographic and the FWI models, respectively. We invert the velocity model from FWI
 224 down to a maximum 9 km depth (~ 5.4 km from basement at distance 182 km), because of

225 potential Moho reflection interference for greater depths (Figs. S23, S24). (b) A schematic
226 diagram illustrating the oceanic crustal structure at the MAR and away from the ridge axis.

227

228 **References**

- 229 1. Morgan, J. P., & Chen, Y. J. The genesis of oceanic crust: Magma injection,
230 hydrothermal circulation, and crustal flow. *J. Geophys. Res. Solid Earth* **98**, 6283-6297
231 (1993).
- 232 2. Cannat, M. et al. Thin crust, ultramafic exposures, and rugged faulting patterns at the
233 Mid-Atlantic Ridge (22–24 N). *Geology* **23**, 49-52 (1995).
- 234 3. Christeson, G. L., Goff, J. A., & Reece, R. S. Synthesis of Oceanic Crustal Structure
235 From Two-Dimensional Seismic Profiles. *Rev. Geophys.* **57**, 504-529 (2019).
- 236 4. Cannat, M. Emplacement of mantle rocks in the seafloor at mid - ocean ridges. *J.*
237 *Geophys. Res. Solid Earth* **98**, 4163-4172 (1993).
- 238 5. Grevemeyer, I., Hayman, N.W., Peirce C., Schwardt M., Van Avendonk H.J.A.,
239 Dannowski A., Papenberg C. Episodic magmatism and serpentinized mantle exhumation
240 at an ultraslow-spreading centre, *Nat. Geosci.* **11**, 444-448 (2018).
- 241 6. Harding, A. J., Kent, G. M., & Orcutt, J. A. A multichannel seismic investigation of upper
242 crustal structure at 9° N on the East Pacific Rise: Implications for crustal accretion. *J.*
243 *Geophys. Res. Solid Earth* **98**, 13925-13944 (1993).
- 244 7. Toomey, D. R., Solomon, S. C., & Purdy, G. M. Tomographic imaging of the shallow
245 crustal structure of the East Pacific Rise at 9° 30' N. *J. Geophys. Res. Solid Earth* **99**,
246 24135-24157 (1994).

- 247 8. Seher, T. et al. Crustal velocity structure of the Lucky Strike segment of the Mid -
248 Atlantic Ridge at 37° N from seismic refraction measurements. *J. Geophys. Res. Solid*
249 *Earth* **115**, B03103 (2010).
- 250 9. Audhkhasi, P., & Singh, S. C. Seismic Structure of the Upper Crust From 0–75 Ma in the
251 Equatorial Atlantic Ocean on the African Plate Using Ultralong Offset Seismic
252 Data. *Geochem. Geophys. Geosyst.* **20**, 6140-6162 (2019).
- 253 10. Hyndman, R. D., Langseth, M. G., & Von Herzen, R. P. Deep Sea Drilling Project
254 geothermal measurements: a review. *Rev. Geophys* **25**, 1563-1582 (1987).
- 255 11. Wilson, D. S. et al. Drilling to gabbro in intact ocean crust. *Science* **312**, 1016-1020
256 (2006).
- 257 12. Müller, R. D., Sdrolias M., Gaina C., and Roest W. R. Age, spreading rates, and
258 spreading asymmetry of the world's ocean crust, *Geochem. Geophys. Geosyst.* **9**, Q04006
259 (2008).
- 260 13. Vaddineni, V.A., Singh, S.C., Grevemeyer, I., Audhkhasi P., & Papenberg C. Evolution
261 of the Crustal and upper Mantle seismic structure from 0 – 27 Ma in the equatorial
262 Atlantic Ocean at 2° 43'S. Submitted to *J. Geophys. Res. Solid Earth*.
- 263 14. Wang, Z., Singh, S. C., & Noble, M. True-amplitude versus trace-normalized full
264 waveform inversion. *Geophys. J. Int.* **220**, 1421-1435 (2020).
- 265 15. Shipp, R. M., & Singh, S. C. Two-dimensional full wavefield inversion of wide- aperture
266 marine seismic streamer data. *Geophys. J. Int.* **151**, 325-344 (2002).
- 267 16. Detrick, R. S. et al. Seismic structure of the southern East Pacific Rise. *Science* **259**, 499-
268 503 (1993).
- 269 17. Grevemeyer, I., Ranero, C.R., and Ivandic, M. Structure of oceanic crust and
270 serpentinization at subduction trenches: *Geosphere*, 14, 395–418 (2018).

- 271 18. Xu, M., Zhao, X., & Canales, J. P. Structural variability within the Kane oceanic core
272 complex from full waveform inversion and reverse time migration of streamer
273 data. *Geophys. Res. Lett.* **47**, e2020GL087405 (2020).
- 274 19. Singh, S. C., Collier, J. S., Harding, A. J., Kent, G. M., & Orcutt J. A. Seismic evidence
275 for a hydrothermal layer above the solid roof of the axial magma chamber at the southern
276 East Pacific Rise. *Geology* **27**, 219-222 (1999).
- 277 20. Boudier, F., Nicolas, A., & Ildefonse, B. Magma chambers in the Oman ophiolite: fed
278 from the top and the bottom. *Earth Planet. Sci. Lett.* **144**, 239-250 (1996).
- 279 21. Kelemen, P. B., Koga, K., & Shimizu, N. Geochemistry of gabbro sills in the crust-
280 mantle transition zone of the Oman ophiolite: Implications for the origin of the oceanic
281 lower crust. *Earth Planet. Sci. Lett.* **146**, 475-488 (1997).
- 282 22. Canales, J. P. et al. Network of off-axis melt bodies at the East Pacific Rise. *Nat. Geosci.*
283 **5**, 279-283 (2012).
- 284 23. Marjanović M. et al. A multi-sill magma plumbing system beneath the axis of the East
285 Pacific Rise. *Nat. Geosci.* **7**, 825-829 (2014).
- 286 24. Arnulf, A. F., Singh, S. C., & Pye, J. W. Seismic evidence of a complex multi- lens melt
287 reservoir beneath the 9° N Overlapping Spreading Center at the East Pacific Rise.
288 *Geophys. Res. Lett.* **41**, 6109-6115 (2014).
- 289 25. Carbotte, S. M. et al. Stacked sills forming a deep melt-mush feeder conduit beneath
290 Axial Seamount. *Geology* **48**, 693-697 (2020).
- 291 26. Canales, J. P., Nedimović, M. R., Kent, G. M., Carbotte, S. M., & Detrick R. S. Seismic
292 reflection images of a near-axis melt sill within the lower crust at the Juan de Fuca ridge.
293 *Nature* **460**, 89-93 (2009).

- 294 27. Dunn, R. A., Lekić, V., Detrick, R. S., & Toomey, D. R. Three - dimensional seismic
295 structure of the Mid - Atlantic Ridge (35° N): Evidence for focused melt supply and
296 lower crustal dike injection. *J. Geophys. Res. Solid Earth* **110**, B09101 (2005).
- 297 28. VanTongeren, J. A., Kelemen, P. B., & Hanghøj, K. Cooling rates in the lower crust of
298 the Oman ophiolite: Ca in olivine, revisited. *Earth Planet. Sci. Lett.* **267**, 69-82 (2008).
- 299 29. Casey, J. F., & Karson, J. A. Magma chamber profiles from the Bay of Islands ophiolite
300 complex. *Nature* **292**, 295-301 (1981).
- 301 30. Natland, J. H., Dick, H. J. B., Miller, D. J., & Von Herzen, R. P. Velocity structure of the
302 lower oceanic crust: results from Hole 735B, Atlantic II Fracture Zone. In *Proc. ODP,*
303 *Sci. Results* **176**, 1-71 (College Station, Tex.: Ocean Drilling Program. 2001)
- 304 31. Boulanger, M. et al. Magma reservoir formation and evolution at a slow-spreading center
305 (Atlantis Bank, Southwest Indian Ridge). *Front. Earth Sci.* **8**, 554598 (2020).
- 306 32. Lissenberg, C. J., MacLeod, C. J., Howard, K. A., & Godard, M. Pervasive reactive melt
307 migration through fast-spreading lower oceanic crust (Hess Deep, equatorial Pacific
308 Ocean). *Earth Planet. Sci. Lett.* **361**, 436-447 (2013).
- 309 33. Carlson, R. L., & Jay Miller, D. Influence of pressure and mineralogy on seismic
310 velocities in oceanic gabbros: Implications for the composition and state of the lower
311 oceanic crust. *J. Geophys. Res. Solid Earth* **109**, B09205 (2004).
- 312 34. Maclennan, J., Hulme, T., & Singh, S. C. Thermal models of oceanic crustal accretion:
313 Linking geophysical, geological and petrological observations. *Geochem. Geophys.*
314 *Geosyst.* **5**, Q02F25 (2004).
- 315 35. Quick, J. E., & Denlinger, R. P. Ductile deformation and the origin of layered gabbro in
316 ophiolites. *J. Geophys. Res. Solid Earth*, **98**, 14015-14027 (1993).
- 317 36. Singh, S. C., & McKenzie, D. Layering in the lower crust. *Geophys. J. Int.* **113**, 622-628
318 (1993).

319

320 **Methods**

321 **Data acquisition**

322 The field OBS data was acquired during the LITHOS-iLAB cruise in November-December
323 2017 onboard the Germain R/V Maria S. Merian to study the upper lithosphere from 0-50 Ma
324 in the study region³⁷. A total of 71 instruments consisting of 55 ocean bottom seismometers
325 (OBSs) and 16 ocean bottom hydrophones (OBHs) were deployed along a 1100-km long
326 transect with a variable spacing of 10-20 km to record wide-angle refractions and reflection
327 arrivals. The majority of the profile (~1000 km) lies on the African Plate (0-50 Ma) and
328 crosses the ridge-axis on to the South American Plate (0-2 Ma) for ~75 km. All OBSs were
329 equipped with a hydrophone (measuring pressure) and three geophones (measuring vertical
330 and horizontal displacements) whereas the OBHs measured only the pressure. The data was
331 sampled at 250 Hz. The active seismic source used in the survey comprised of 6 G-gun
332 clusters (12 guns) configured as two sub-arrays with a total volume of 5440 cubic inch, which
333 was towed at 7.5 m in depth and fired every ~400 m along the profile. The relatively large
334 shot spacing was chosen to reduce the noise from neighbouring shots and hence enhancing
335 the signal-to-noise ratio for farther offsets. We used a part of these data (8 OBSs, pressure
336 component) where the OBS spacing was dominantly ~10 km covering 7-12 Ma old oceanic
337 crust (Fig. 1 and Fig. S1).

338 **Data pre-processing**

339 We limit the data pre-processing to a minimum to keep the waveform information, including
340 a zero-phase bandpass filtering of 3.5 - 10 Hz, and 3D to 2D transformation^{15,38} (multiplying
341 the amplitudes of field data by \sqrt{t} , where t is the two-way travel-time, and convolving with

342 $1/\sqrt{t}$) because 2D elastic wave equation modelling was used for simulating seismic data
343 recorded in a 3D earth. A predictive deconvolution was applied to suppress the bubble effects
344 from the air gun sources. Clear crustal turning waves (Pg) with high signal-to-noise ratio can
345 be observed starting from offsets (source-receiver distance) $\pm 6 - 8$ km, up to offsets of $\pm 20 -$
346 26 km, followed by wide-aperture Moho reflection (PmP) and upper mantle refraction (Pn) at
347 the far offsets. An OBS gather (OBS 58) is shown in Fig. S2, with Pg, PmP, and Pn arrivals
348 labelled.

349 **Travel time tomography**

350 Travel time tomography^{13,39} was first applied to the OBS gathers for estimating a P wave
351 velocity model (Fig. 2a). Travel times of Pg, PmP and Pn were hand-picked with an
352 uncertainty of 30 ms. Tomography was carried out through a linearised approach by updating
353 velocity models iteratively³⁹. At each iteration, a ray-tracing algorithm with a hybrid of graph
354 (shortest path) method and ray bending for further refinements was used for forward
355 modelling of travel times; the model update (the partial derivatives of travel times to the
356 model parameters) was obtained by least-squares penalties on the data misfit, together with
357 smoothing and damping for regularising the inversion problem³⁹.

358 The velocity model from travel time tomography gives very good travel-time fit for the first
359 arrival¹³. Since the travel time is mainly sensitive to large-scale velocity structures, the
360 tomographic velocity model contains few details for the oceanic crust. The first arrival, Pg,
361 rays penetrate down to ~ 3 km below the seafloor, thus the velocity in the lower crust is
362 mainly determined using PmP arrivals, which is poorly constrained because of the trade-off
363 between the lower crustal velocity and the Moho depth. Details of the travel-time tomography
364 can be found in Vaddineni et al (2020)¹³.

365

366 **Full waveform inversion (FWI)**

367 FWI is the current state-of-the-art technique for high-resolution subsurface imaging^{15,37,38}.

368 We adopted the approach of time-domain finite-difference elastic FWI¹⁵ for improving the

369 tomographic model. Unlike travel-time tomography that relies on minimizing the travel time

370 from high-frequency approximated ray-tracing³⁹, the FWI is based on minimising the

371 difference between the observed and synthetic seismic waveforms, with a numerical solution

372 of the elastic wave-equation for realistic simulation of seismic wave propagation in the

373 frequency band of interest^{15,38}. For the numerical implementation, a gradient-based linearised

374 inversion approach is used for updating the velocity model iteratively, with the gradients of

375 the data misfit to model parameters efficiently calculated by the adjoint method from cross-

376 correlation of the forward and adjoint wavefields^{15,38}.

377 The capability of recovering high-resolution crustal images using the FWI comes from the

378 fact that the amplitudes and waveforms of the recorded wavefield are more sensitive to fine-

379 scale geological features than travel time. It also has the potential of being sensitive to crustal

380 structures at greater depth than travel-time tomography, with the increased depth coverage

381 attributed to a wavelength of ~ 1.2 km from finite-bandwidth waveform (a dominant

382 frequency of 6 Hz with ~ 6.8 km/s P-wave velocity in the lower crust) rather than a high-

383 frequency approximated ray path. Furthermore, other wide-angle arrivals, e.g. weak

384 reflections from the lower crust, are included in the waveforms.

385 Although the tomographic inversion using ray-trace modelling has converged with good

386 travel-time fit¹³, large waveform difference can be observed between the field data and the

387 synthetic seismograms from wave-equation modelling (Fig. 3, Figs. S7-S10). Hence, we

388 employed a multi-stage strategy for obtaining the final model. In the first stage of FWI, the

389 tomographic model was used as the starting model. A trace-normalised FWI¹⁴ was applied,
390 where the amplitudes of each trace within a common OBS gather were normalised by the
391 norm-2 of the trace itself. This may be considered as a bridge between tomography and
392 classic FWI using ‘true amplitude’ waveform: the influence of amplitude-versus-offset is
393 removed by trace-by-trace normalisation and the inversion mainly focuses on fitting the
394 phase information simulated from elastic wave-equation modelling. From trace-normalised
395 FWI, we were able to obtain an improved crustal model (Fig. S3). In the second stage, we
396 performed a true-amplitude FWI^{15,38}, with the waveform misfit between field and synthetic
397 data being the objective function for minimisation. The inversion was carried out using a top-
398 down approach: we inverted first for the relatively shallow structures, which were
399 constrained by near-to-intermediate source-receiver offset ranges (from ± 6 -8 km up to ± 15
400 km offsets) of crustal Pg arrivals, then far-offset arrivals were included for estimating the
401 deeper crustal model. The updated velocity model from the prior stage was used as the
402 starting model for the next stage of inversion, and the final results after a total of 80 iterations
403 are shown in Fig. S4.

404 For the inversion, we only used crustal Pg arrivals, because this part of data has the most
405 linear behaviour in FWI and the wide-aperture data is sensitive to both the upper- and lower-
406 crustal structures. We didn’t apply FWI to the PmP arrivals, because of its strong nonlinearity
407 around critical angles. A time-window of 0.5 s was applied to the OBS gathers, by muting the
408 data before 0.2 s, and after 0.3 s of the picked Pg travel times, to reduce the influence of
409 noise, and to isolate Pg arrivals from the other seismic events. A careful visual inspection was
410 then performed to further mute data at far offsets when the Pg, PmP and Pn arrivals overlap,
411 to reduce potential interference from Moho and mantle related seismic phases in the time
412 window. Since the Pg arrivals do not have information for updating the S-wave velocities, we
413 updated the P-wave velocity model only, with the S-wave velocity model derived from the P-

414 wave velocity using Brocher's regression fit⁴⁰. The finite-difference modelling algorithm
415 used a grid spaced at 20 m for both the horizontal and vertical directions, which can ensure
416 the accuracy for propagating P waves with frequency range below 15 Hz. Considering the
417 sparse distribution of OBS on the seafloor, a gaussian smoothing operator (4 km and 0.4 km
418 in the horizontal and vertical directions, respectively) was applied to the gradient for gradient
419 regularisation.

420 Source wavelet for wave equation modelling was estimated by stacking near-offset free-
421 surface multiples of water waves³⁷, thanks to a good separation between water waves and
422 seafloor-related scatterings in their free-surface multiples. An amplitude scaling factor was
423 then estimated by comparing the field and synthetic Pg waveforms at near offsets.

424 Velocity anisotropy was not taken into consideration for the FWI in the present study.
425 Although oceanic crust contains highly anisotropic minerals, their random orientation makes
426 the oceanic crust nearly isotropic, which is supported by evidence from Hole 735B for the
427 lower crust³⁰. Studies near the ridge axis indicate anisotropy of 1%-2% at the top 3 km depth
428 on the MAR³. The observed anisotropy is attributed to vertical cracks aligned with the ridge
429 axis, and decreases fast off-axis over 5-10 km. Therefore, we consider the influence of
430 anisotropy from upper and lower crust between 7-12 Ma negligible.

431 In order to heighten the salient features of the results from trace-normalised (Fig. S3) and
432 true-amplitude (Fig. S4) FWI, besides the velocity models, we also show the velocity
433 anomalies (the difference between the tomographic and the FWI models) as well as the
434 vertical velocity gradients. For example, the velocity anomaly from the trace-normalised FWI
435 highlights the large-scale velocity variations between the upper and lower crust (Fig. S3b),
436 whereas the vertical velocity gradient from the true-amplitude FWI enhances the layered
437 structures in the lower crust (Fig. S4c), therefore these figures are presented in Fig. 2.

438 Fig. S5 shows one-dimensional (1-D) velocity-depth profiles below basement between 112
439 km and 192 km distance along the profile from the tomographic and FWI velocity models.
440 One can observe that there is a wider variation in velocity both in the upper and lower crust
441 as compared to the tomographic results, with layering in the lower crust along the whole
442 model, although the depths of these layers vary along the profile. A subset of two (1-D)
443 velocity-depth profiles are shown in Fig. S6, with the interpreted boundaries of Layer 2A/2B
444 and 2/3. Figs. S7 to S10 show seismic waveforms for the observed data, the initial synthetic
445 seismograms computed using the tomographic model, and synthetic seismograms from the
446 inverted FWI model, indicating much improved waveform match between the observed and
447 synthetically computed data after FWI when compared with the tomographic results.
448 Waveform fitness from FWI at far offsets is generally better than that at relatively near
449 offsets; the reasons could be that small anomalies in the upper crust is not well resolved by
450 sparse OBS data, and there are fewer constraints for the topmost crust from the Pg arrivals.
451 The norm-2 misfit after FWI was reduced by 36%.

452 **Resolution and uncertainty synthetic studies**

453 In order to gain confidence in our results, especially for the layered structures in the lower
454 crust, we performed several numerical tests by modifying the velocity model with different
455 scenarios of anomalies, and then applied FWI using the same source and receiver positions
456 and frequency ranges of the data as in the actual observation, and the same inversion
457 parameters. We also tested the potential influence of Moho reflections (PmP).

458 In the first of these tests, we modified the velocity model from FWI starting from 5.8 km
459 depth to the bottom of the model (Fig. S11), by replacing the layering structures with the
460 corresponding tomographic model in order to see if the layered structures in the lower crust
461 are required by the data and not due to smearing of the structures in the upper crust. Fig. S13a

462 shows a comparison of synthetic seismograms using the modified model and field data,
463 without layering in the lower crust; larger waveform misfit than Fig. 3b can be observed at
464 far (larger than 20 km) offsets, the propagation paths of which sample the lower crust. We
465 used the modified model as the starting model for FWI. The inverted model is shown in Fig.
466 S12 with remarkable similarity to Fig. S4; the waveform match is much better in Fig. S13b
467 than Fig. S13a for far offsets. This test suggests that the layered structure in the lower crust is
468 required for explaining the crustal Pg arrivals in the data.

469 Then we wanted to estimate the size of the anomaly that could be recovered using our FWI
470 settings. We began with checkerboard tests. Although not comprehensive, this is a succinct
471 and computationally efficient approach to demonstrate the resolution of FWI using available
472 data, therefore has been widely used for studying inversion problems. We generated synthetic
473 models by adding 8% positive and negative Gaussian-shaped velocity anomalies to the
474 tomographic velocity model. Fig. S14a shows the true velocity anomalies; each of the
475 Gaussian anomalies is 10 km long and 1 km thick. The perturbed velocity model was then
476 used for generating the ‘observed’ data for the inversion. We used the unperturbed
477 tomographic model as the starting model for the FWI to see how well these perturbations can
478 be recovered. The same procedure was applied for a second checkerboard test, with the only
479 difference being that the Gaussian anomalies have 0.5 km thickness (Fig. S15a). The inverted
480 velocity anomalies in Figs. S14b and S15b show good match with the true models, with
481 resolution for both the upper and lower crust on the scale of 10 km laterally and 500 m
482 vertically, consistent with OBS spacing and the frequency content of the data.

483 The next set of tests were to see what kind of layered structures in the lower crust that could
484 be resolved from the FWI. Five synthetic studies were performed. We perturbed the velocity
485 model, by adding five types of layered velocity anomalies shown in Figs. S16a-S20a,

486 respectively. The layering model in Fig. S16a contains alternating high and low velocity
487 anomalies of ± 200 m/s with 500 m layer thickness; Fig. S17a contains high and low velocity
488 anomalies of ± 200 m/s with a transitional gradient of 1 s^{-1} ; the velocity anomalies in Fig.
489 S18a correspond to the gradational layering with 500 m thickness for each layer, where the
490 velocity increases linearly to 350 m/s and then sharply decreases to the background velocity
491 at its base; the layering model in Fig. S19a are step-wise positive velocity anomalies with 500
492 m layer thickness, with a velocity increase of 200 m/s; finally, the layering model in Fig.
493 S20a is a low velocity anomaly of - 300 m/s and 400 m thickness with a Gaussian-shape
494 transition boundary.

495 Because of the band-limited frequency of the data, a smoothed version of the models in Figs.
496 S16b-S20b were recovered by FWI. These tests provide evidence that the wide-aperture Pg
497 arrivals are capable of constraining the layering structure for high and lower velocity
498 anomalies (Figs. S16, S17, S20). The inverted model in Fig. S18b shows the increasing
499 velocity pattern, although unable to reconstruct the sharp step boundaries. Fig. S19 indicates
500 that the gradational layering structure cannot be resolved with high resolution by crustal Pg
501 arrivals; instead, an average model is obtained. There are inversion artifacts in the vicinity of
502 inverted anomaly boundaries, arising from the side lobes of seismic data. Fig. S21 shows
503 velocity-depth functions at 168 km distance from Figs. S16-S20, highlighting the above
504 points, and indicates that the layering velocity model in the lower crust can be well resolved
505 and is required by the field OBS data.

506 We also tested if the layering in the lower crust could be introduced by the potential presence
507 of the Moho (PmP) reflections in the windowed data containing mainly crustal Pg arrivals.
508 We used the velocity model with Moho (Fig. S22a)¹³ for generating the ‘observed’ data. For
509 FWI, the velocity model after removing the Moho and upper mantle (Fig. S22b, the velocities

510 of these parts were replaced by velocities immediately above the Moho) was used as the
511 starting model. A larger time window, between 0.2 s before and 0.5 s after the picked Pg
512 travel times, than that for field data FWI, was used for including both the Pg and PmP
513 arrivals. Fig. S23 shows the inverted velocity model, the velocity anomaly (the difference
514 between the inverted model and the starting model), and the vertical velocity gradient. The
515 PmP arrivals focused around Moho depths as expected, with weak artifacts in the crust. The
516 velocity anomalies contain mainly positive values, with negative sidelobes at crustal base
517 arising from the band-limited nature of seismic data. In a second test, we used the same
518 window size as for field data FWI, for containing mainly the Pg arrivals for inversion. The
519 inversion results are shown in Fig. S24. We observed weaker anomalies around the crustal
520 base, indicating that the windowed data may contain certain PmP arrivals at far offsets, but
521 their influence for the observed crustal layering is limited. These tests confirm that the Moho
522 reflection is unlikely attributed to the layering structures in the lower crust, especially for
523 those away from the base of crust; and the layering model in the lower crust away from the
524 crustal base represents real features of the sub-surface.

525 **Voigt-Reuss-Hill averaging for rock property modelling**

526 In order to shed light on the types of rocks that can produce velocities comparable to those
527 estimated from the FWI study, we estimated velocities for rocks commonly present in the
528 lower crust. Voigt-Reuss-Hill (VRH) averaging⁴¹ is a common and simple approach for
529 computing the effective elastic moduli of rock from the volume fractions and elastic
530 properties of their mineral constituents. Evidence³⁰⁻³³ from IODP/ODP drilling and ophiolite
531 show that the gabbroic rocks of the lower crust are mainly composed of olivine (Ol),
532 clinopyroxene (Cpx), and plagioclase (Pl). Therefore, we calculated the P-wave velocities
533 using different combinations of Ol, Cpx and Pl volume fractions. The elastic moduli and

534 densities⁴² of the three mineral components shown in Table S1. We expect the velocities to
535 increase with increasing Ol or Cpx, and decrease with increasing Pl. By varying the volume
536 fractions of different components, we found a velocity variation of 200-400 m/s (\pm 100-200
537 m/s, Table S2), similar to those observed from the FWI. Pyroxene may play a more important
538 role in increasing the velocities of gabbro than Ol, because the properties of Ol can get more
539 easily altered leading to low effective densities and elastic moduli³³. In the case of the
540 properties of Ol being altered in our study area, similar amount of alternation of Cpx volume
541 fraction can produce the P-wave velocity variations as observed in the FWI model, because
542 the properties of Ol and Cpx are relatively close.

543

544 **Data availability**

545 The raw OBS data used for this study is stored at the PANGAEA Data center
546 <https://doi.pangaea.de/10.1594/PANGAEA.914912>. The processed OBS data and the
547 derived velocity models can be accessed at <https://zenodo.org/deposit/4390552>.

548 **Code availability**

549 The code for travel-time tomography and full waveform inversion can be accessed upon
550 reasonable request from Singh.

551 **Acknowledgements**

552 The OBS data were acquired during the LITHOS-iLAB experiment on board the German
553 R/V Maria S. Merian in 2017. We thank Dr Lydéric France for the discussion on ODP Hole
554 735B. This project was funded by the European Research Council Advanced Grant
555 agreement No. 339442 TransAtlanticILAB. The cruise with the ID MSM69 was funded by

556 the German Science Foundation (DFG). This research was funded by the Deep Earth Imaging
557 Future Science Platform, CSIRO. This work was supported by resources provided by the
558 Pawsey Supercomputing Centre with funding from the Australian Government and the
559 Government of Western Australia. We also thank the computational resources supported by
560 S-CAPAD at IPG Paris. The maps were plotted using open software GMT 6.0.0, and the
561 other figures were created using open software Python 2.7 with Matplotlib 3.1.0.

562 **Author contributions**

563 P.G. performed data processing and full waveform inversion of the OBS data, analysed the
564 results, and wrote the paper; S.C.S. participated in the OBS data acquisition, designed and
565 supervised the project, interpreted the results, and wrote the paper; V.A.V. participated in the
566 OBS data acquisition, performed data processing and travel-time tomography; I.G. led the
567 OBS data acquisition; E.S. analysed the results.

568 **Competing interest declaration**

569 The authors declare no competing interests.

570 **Additional information**

571 Supplementary information is available for this paper. Correspondence and requests for
572 materials should be addressed to Guo.

573

574 37. Guo, P., Singh, S. C., Vaddineni, V. A., Visser, G., Grevemeyer, I., & Saygin, E.

575 Nonlinear full waveform inversion of wide-aperture OBS data for Moho structure using a
576 trans-dimensional Bayesian method. *Geophys. J. Int.* **224**, 1056-1078 (2021).

- 577 38. Tarantola, A. Inversion of seismic reflection data in the acoustic approximation. *Geophys.*
578 **49**, 1259-1266 (1984).
- 579 39. Van Avendonk, H. J., Harding, A. J., Orcutt, J. A., & McClain, J. S. A two- dimensional
580 tomographic study of the Clipperton transform fault. *J. Geophys. Res. Solid Earth* **103**,
581 17885-17899 (1998).
- 582 40. Brocher, T. M. Empirical relations between elastic wavespeeds and density in the Earth's
583 crust. *Bull. Seismol. Soc. Am.* **95**, 2081-2092 (2005).
- 584 41. Hill, R. The elastic behaviour of a crystalline aggregate. *Proc. Phys. Soc., A.* **65**, 349
585 (1952).
- 586 42. Sobolev, S. V., & Babeyko, A. Y. Modeling of mineralogical composition, density and
587 elastic wave velocities in anhydrous magmatic rocks. *Surv. Geophys.* **15**, 515-544 (1994).

Figures

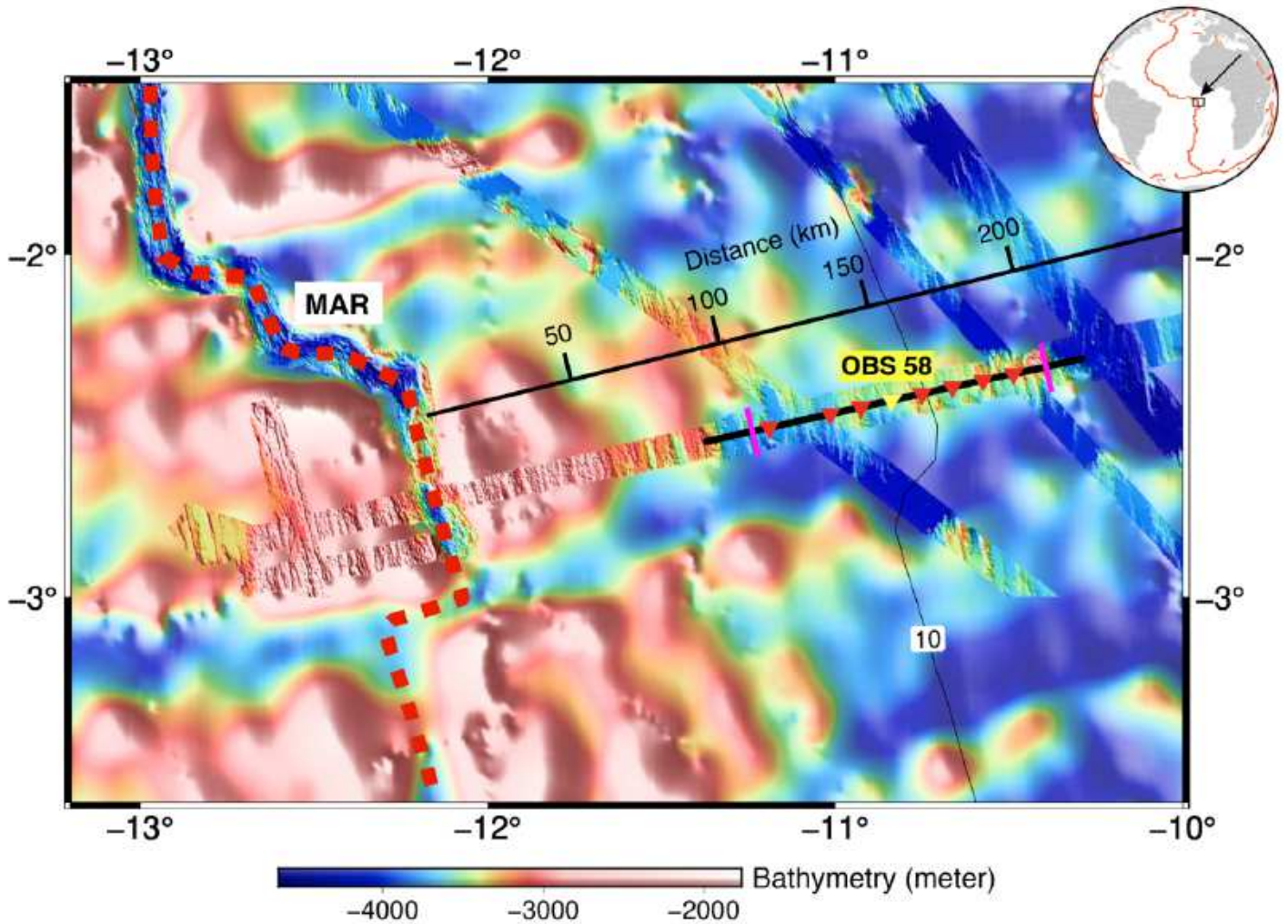


Figure 1

Study Area: The ocean bottom seismometer (O 39 BS) seismic survey near the Mid-Atlantic Ridge (MAR) in the equatorial Atlantic Ocean. The dashed red line refers to the MAR, and the triangles show the locations of the OBSs used for this study. OBS 58 (yellow triangle) is labelled, with the seismograms shown in Fig. 3. The bold black line passing through OBSs shows the part of shot profile used, and the two pink bars indicate the boundaries of the seismic images shown in Fig. 2. The thin black line and numbers indicate the distance from the MAR. The contour labelling 10 indicates the 10 Ma lithospheric age. See the inset map for the location of the study area.

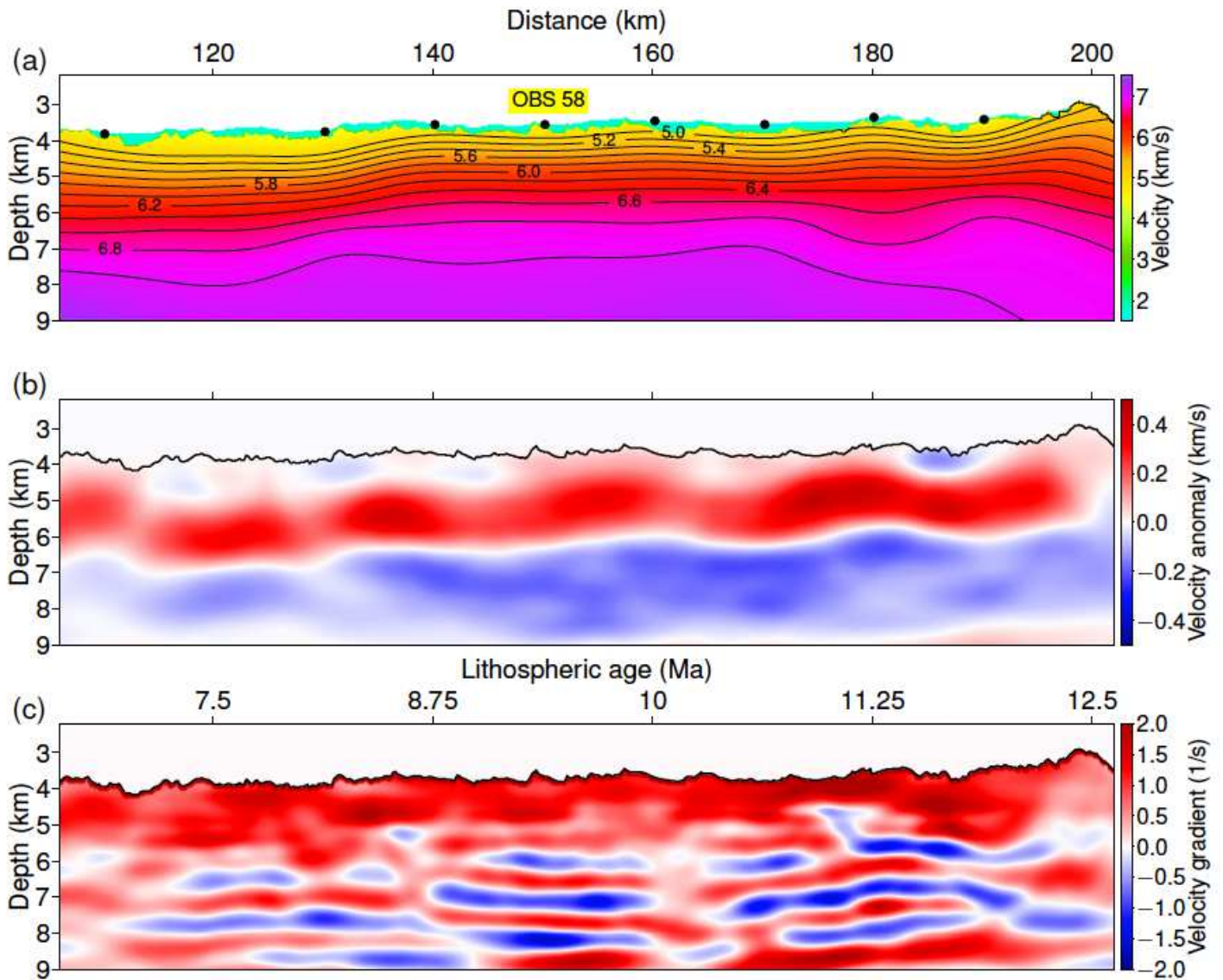


Figure 2

Velocity Models: (a) The tomographic seismic velocity model¹³ serves as the starting model for the FWI, (b) the velocity anomaly (the difference between the velocity models from FWI and tomography) from the trace-normalised FWI¹⁴, and (c) the vertical velocity gradient (the derivative of velocity with respect to depth) from the 'true amplitude' FWI¹⁵. Black dots in (a) mark the OBS locations. The velocity contours are from 5 to 7 km/s with an increment of 0.2 km/s. The coloured parts in (b) and (c) start from the basement (the top of Layer 2). The lithospheric age in (c) is calculated using a spreading rate of 16 mm/year¹². More images of the oceanic crustal velocity models from FWI can be found in Figs. S3 and S4. The horizontal distance starts with 0 km from the MAR.

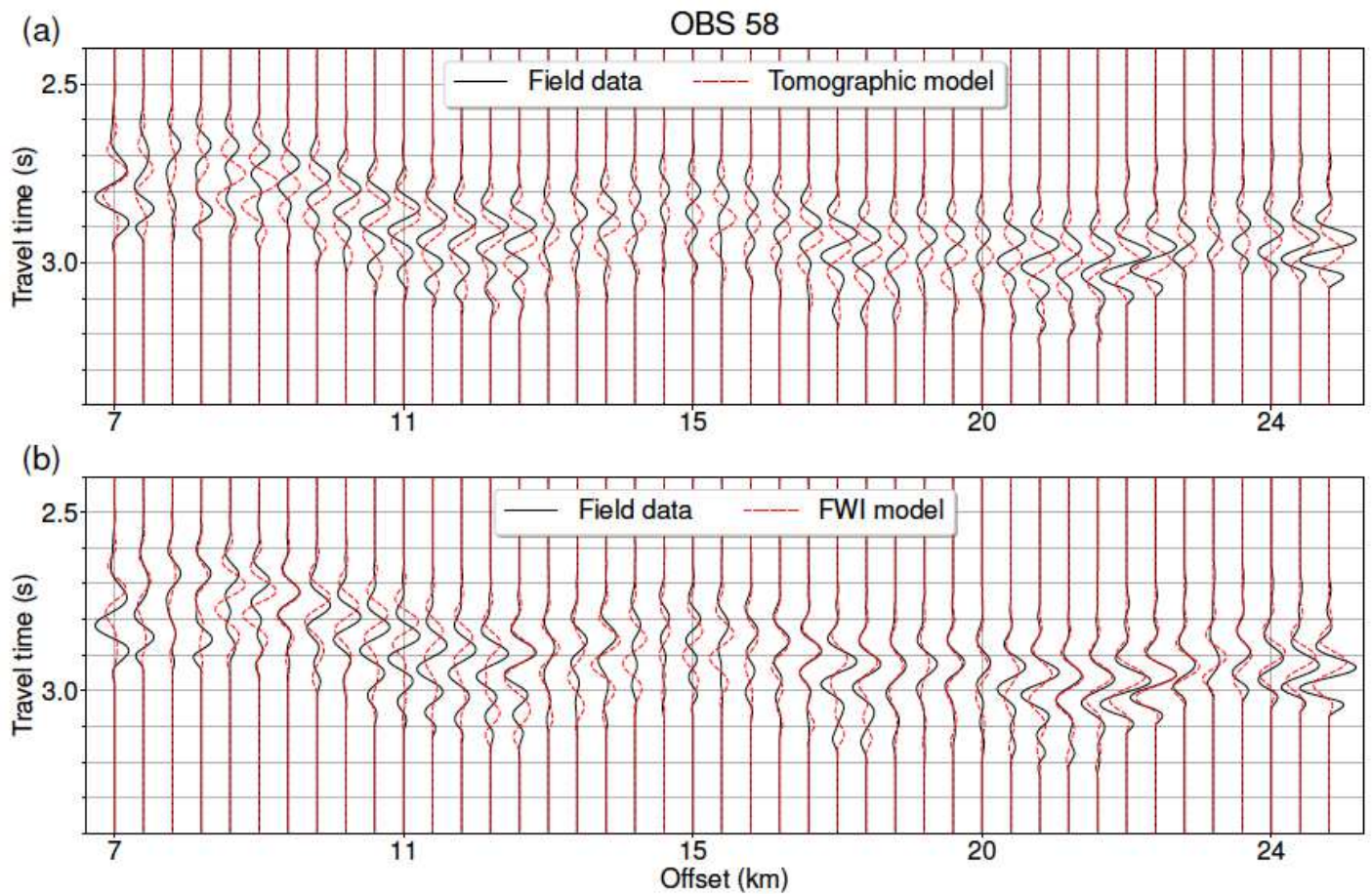


Figure 3

Data comparison for OBS 58: (a) The field data (black) and the synthetic waveform (red) using the tomographic model (Fig. 2a), and (b) the field data (black) and the synthetic waveform (red) using the true-amplitude FWI model (Fig. S4a). Seismic waveforms from more OBSs can be found in Figs. S7-S10. A reduced travel time of 7 km/s velocity was applied to both the field and synthetic data for plotting purpose.

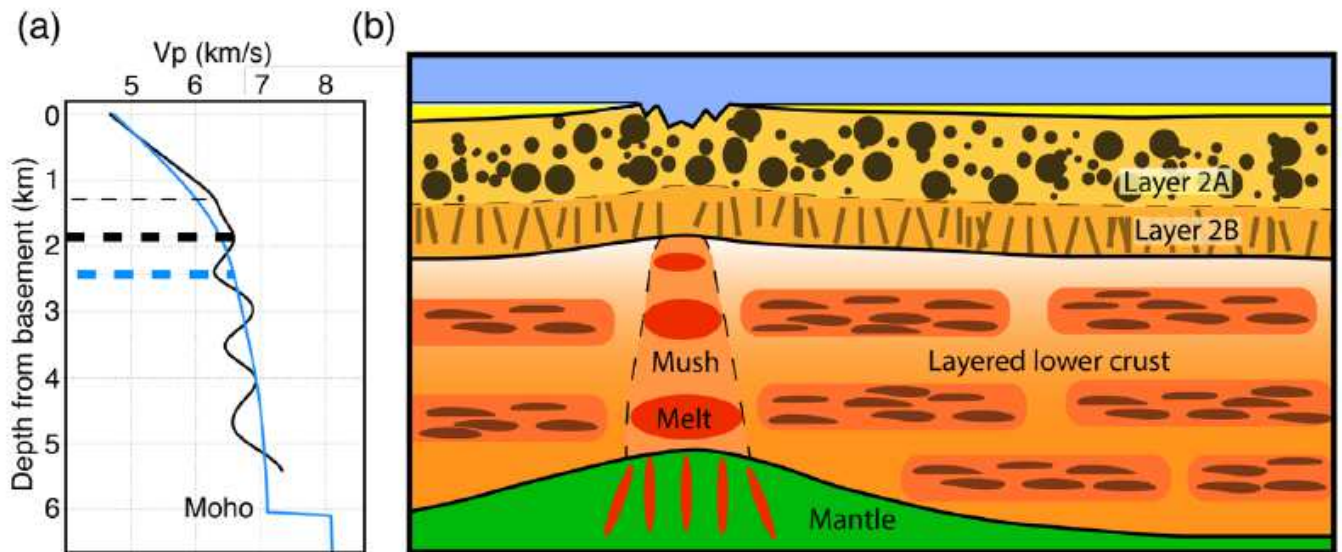


Figure 4

Layering in the lower crust: (a) One-dimensional velocity-depth profiles at the distance of 182 km from the MAR, derived from tomography (blue) and FWI (black), respectively. The thin dashed black line is the interpreted boundary of Layer 2A/2B from the FWI model; the bold dashed blue and black lines indicate the boundaries of Layer 2/3 from the tomographic and the FWI models, respectively. We invert the velocity model from FWI down to a maximum 9 km depth (~5.4 km from basement at distance 182 km), because of potential Moho reflection interference for greater depths (Figs. S23, S24). (b) A schematic diagram illustrating the oceanic crustal structure at the MAR and away from the ridge axis.

Supplementary Files

This is a list of supplementary files associated with this preprint. Click to download.

- [Supplementaryfinalfinal.pdf](#)